Upper-plate Shortening and Mountain-building in the Context of Mantle-driven Oceanic Subduction

Tania Habel, Anne Replumaz, Benjamin Guillaume, Martine Simoes, Thomas Geffroy, Jean-Jacques Kermarrec, Robin Lacassin

TEKTONIKA

Upper-plate Shortening and Mountain-building in the Context of Mantle-driven Oceanic Subduction

Tania Habel [1], **Anne Replumaz** *[2], **Benjamin Guillaume** [3], **Martine Simoes** [1], **Thomas Geffroy** [3], **Jean-Jacques Kermarrec** [3], **Robin Lacassin** [1]

[1]Université Paris Cité, Institut de physique du globe de Paris, CNRS, F-75005 Paris, France | [2]Institut des Sciences de la Terre (ISTerre), Université Grenoble Alpes, CNRS, USMB, IRD, IFSTTAR, Grenoble, France | [3]Université de Rennes, CNRS, Géosciences Rennes, UMR 6118, Rennes, France

Abstract The mechanisms controlling mountain building at subduction zones remain debated. In particular the interaction between mantle flow and subduction has been poorly addressed while fundamental in controlling plate displacement and deformation. Here, we conduct three-dimensional analogue models at the scale of the upper mantle adding a horizontal mantle flow, so that plate displacement is not imposed as in most models, but is rather controlled by the balance of forces. We simulate three scenarios: no mantle flow (slab-pull driven subduction), mantle flow directed toward the subducting plate, and mantle flow directed toward the overriding plate. In that last scenario, we test the influence of pre-existing rheological contrasts in the upper plate to best reproduce natural cases where structural and rheological inheritance is common. Our experiments show that when plate convergence is also driven by a background mantle flow, the continental plate deforms with significant trench-orthogonal shortening (up to 30% after 60 Myr), generally associated with thickening. The upper plate shortening and thickening is best promoted when the mantle flow is directed toward the fixed overriding continental plate. The strength of the upper plate is also a key factor controlling the amount and rates of accommodated shortening. Deformation rates increase linearly with decreasing bulk strength of the upper plate, and deformation is mostly localized where viscosity is lower. Finally, we discuss the limits and strengths of our model results through a comparison to the Andes which are the best modern example of mountain building in a subduction context.

Executive Editor:
Janine Kavanagh
Associate Editors:
Noah Phillips
Technical Editor:
Bülent Tokay

Reviewers:
Ágnes Király
Anonymous

Submitted:
27 January 2023
Accepted:
24 August 2023
Published:
1 November 2023

1 Introduction

Upper plate shortening and mountain-building in an oceanic subduction context is somehow a paradox since most of the present-day subduction zones do not show any significant topography besides that related to their active volcanic arc. Indeed, the negative buoyancy of the subducting oceanic plate generally leads to slab roll-back and trench retreat, resulting in the extension of the upper plate as currently observed all over the globe (e.g., Tonga, Ryukyu and Mariana, see *Lallemand et al.*, 2005). In contrast, most of the mountain belts presently observable on Earth, such as the Himalayas or the European Alps, formed in a continental collisional context where two buoyant continental plates converge, one underthrusting the other (e.g., *Replumaz et al.*, 2016). The Andes are an exception and constitute the modern active example of a subduction-type orogeny. Indeed, after a period of classical subduction during most of the Mesozoic, characterized by extensional basins all along the western margin of South America, upper plate shortening and thickening proceeded since the Late Cretaceous-Early Cenozoic to form the present-day Andes (e.g., *Mpodozis and Ramos*, 1990; *Jaillard et al.*, 2000; *Oncken et al.*, 2006; *Armijo et al.*, 2015). Diverse mechanisms have been suggested for this transition to an Andean-type subduction : (a) Strong coupling between the subducting and overriding plates above flat slab segments (e.g., *Martinod et al.*, 2010, 2020), which may result from the relatively young age and buoyancy of the subducting slab (e.g., *Molnar and Atwater*, 1978; *Capitanio et al.*, 2011); (b) Absolute velocity and acceleration of the upper plate toward the subduction trench (e.g., *Sobolev and Babeyko*, 2005; *Guillaume et al.*, 2018; *Wolf and Huismans*, 2019), related to the westward drift of South America. In turn, this drift is driven by mantle flow, and as such is controlled by (a) the dimensions of the South Atlantic convection cell (e.g., *Husson et al.*, 2012; *Faccenna et al.*, 2013), and possibly enhanced by (b) the large size of the subducting slab (e.g., *Schellart et al.*, 2007; *Schellart and Moresi*, 2013; *Schellart*, 2017) and/or (c) the anchoring of the slab into the lower mantle (e.g., *Quinteros and Sobolev*, 2013; *Schellart*, 2017; *Faccenna*

*✉ anne.replumaz@univ-grenoble-alpes.fr

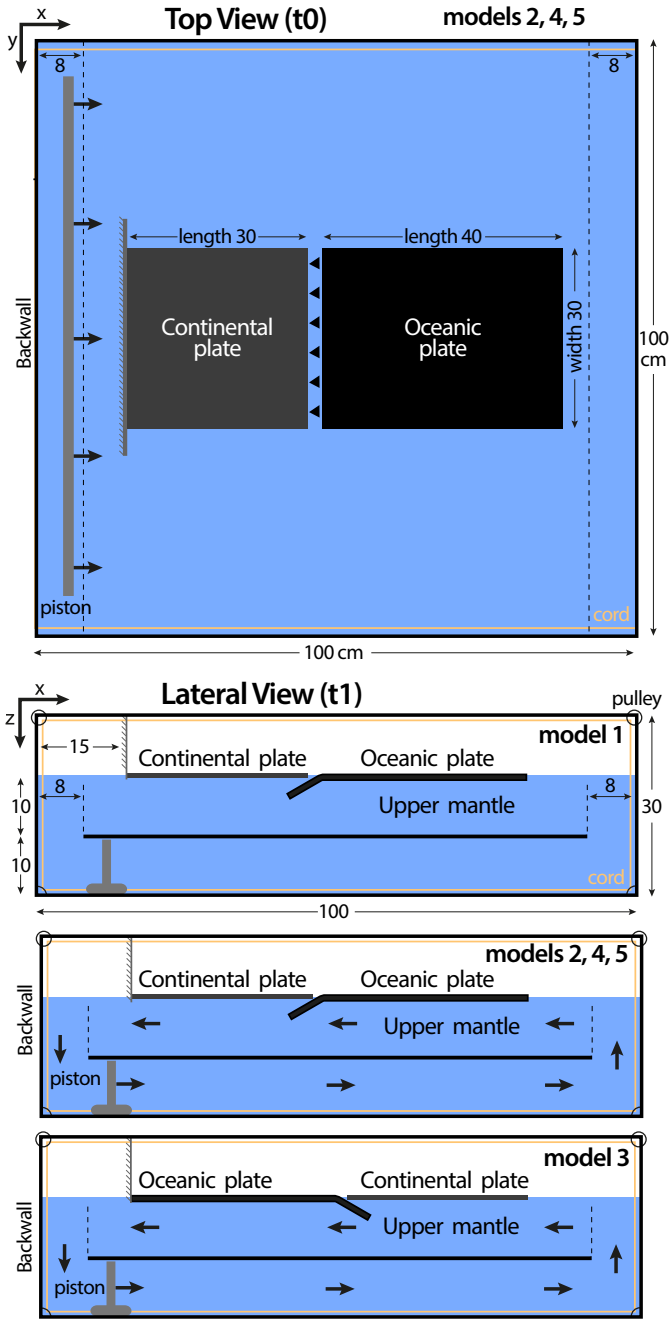

Figure 1 – Top view of the experimental set-up for models 2, 4 and 5, before the start of the experiments (t0) (Upper panel). In the model 3, the position of the plates is inverted, and the oceanic plate is attached to the back wall. In the model 1, the piston controlling mantle flow is not activated. Dimensions are given in cm. Side views of the different experimental set-ups at subduction initiation (t1) (Three lower panels). The mantle flow in the upper part of the model is generated by a motor-driven pulley-cord-system driving a piston-panel moving through the lower part of the model over nearly the entire width of the box (except for model 1).

et al., 2017; *Chen et al.*, 2019). At the lithospheric scale, the slab geometry and the net plate movement, possibly related to the underlying mantle flow, are therefore suspected to be key parameters to produce the Andean subduction orogeny. More generally speaking, upper plate shortening has been inferred along other subduction zones, even though less intense than the emblematic case of the Andes (e.g., *Heuret and Lallemand*, 2005), and found to occur where the mean net trenchward force resulting from the mantle drag beneath the two converging plates is highly positive (e.g., *Husson*, 2012).

To understand the mechanics of converging plate systems, the mantle flow related to the subduction system has to be considered in its 3D complexity, in particular taking into account both the poloidal component of the mantle flow parallel to the slab motion, and the toroidal flow perpendicular to it (e.g., *Dvorkin et al.*, 1993; *Funiciello et al.*, 2004).The spatial scale over which the toroidal and poloidal cells develop has been shown to be dependent on the dimensions of the convective mantle (e.g., *Király et al.*, 2017; *Guillaume et al.*, 2021), and from there indirectly on the along-strike width of a subduction zone (e.g., *Heuret and Lallemand*, 2005; *Strak and Schellart*, 2016; *Hayes et al.*, 2018) or the downdip penetration of the slab into the mantle (e.g., *Holt et al.*, 2015; *Faccenna et al.*, 2017; *Schellart*, 2017). Indeed, subductions extending over a few hundreds of kilometers (e.g., the Caribbean) have mantle flow patterns different from those of the ~8000 km long-lived Andean subduction system, possibly inducing different trench curvatures and kinematics, in line with the different deformation styles observed in their respective upper plates (e.g., *Schellart*, 2008, 2017).

Analogue and numerical modeling has been of great help to understand subduction systems in 3D. When subduction zones are considered as isolated systems where the only driving force is the slab pull associated with the negative buoyancy of the subducting lithosphere, the subduction trench most generally retreats toward the subducting plate (e.g., *Chase*, 1978; *Uyeda and Kanamori*, 1979; *Dewey*, 1980; *Garfunkel et al.*, 1986; *Richards and Engebretson*, 1992; *Funiciello et al.*, 2004), along with overriding plate extension driven by slab-induced mantle flow (e.g., *Meyer and Schellart*, 2013; *Schellart and Moresi*, 2013). If the trench remains almost stationary, backarc shortening can develop because of the shear stresses at the base of the overriding plate that drive it toward the trench (e.g., *Schellart and Moresi*, 2013). This is a condition that can be particularly met after the arrival of the slab at the upper-lower mantle discontinuity (e.g., *Holt et al.*, 2015; *Faccenna et al.*, 2017; *Schellart*, 2017). On the contrary, when subducting plate horizontal displacement is forced by imposing a constant velocity at the trailing edge of the slab, simulating a combination of ridge push and mantle drag at the base of the subducting lithosphere, the slab folds and alternates periods of steepening/shallowing associated with stages of extension/shortening in the overriding plate (e.g., *Guillaume et al.*, 2009; *Gibert et al.*, 2012; *Cerpa et al.*, 2014). However, these experiments with a constant plate velocity cannot fully reproduce a natural system where plate kinematics adjust to the force equilibrium.

In this paper, we build original analogue models of subduction, and consider a scenario in which plates move not only as a result of slab pull, but also because of an imposed underlying mantle flow, and are therefore not considered as isolated systems. Here, plate velocities adjust to the balance of forces in the system, rather than through imposing the kinematics. We build upon the preliminary works by *Guillaume et al.* (2021) which are the first three-dimensional analogue experiments with mantle flow but without an overriding plate and investigate the conditions leading to compressive deformation in the upper plate in the case of such an imposed mantle flow. We also characterize how this deformation is distributed within the upper plate, testing the effects of laterally variable strength. We finally compare to the first order, our experimental results to the emblematic natural case example of the Central Andes.

2 Methods

2.1 Experimental set-up

The experimental apparatus has been specifically designed to model subduction driven by background flow in the upper mantle (Figure 1). The model box is a 100 x 100 x 30 cm^3 plexiglass tank filled with glucose syrup, taken as an analogue material for the sub-lithospheric mantle. A horizontal 1 cm thick intermediate plexiglass layer fixed to two of the tank walls, simulates an impermeable limit between the lower and upper mantles. On the two other sides of the box, an 8 cm gap between the wall and this horizontal layer enables the circulation of the glucose syrup in between the two compartments. Trench-perpendicular unidirectional horizontal mantle flow is generated in the upper part of the tank (upper mantle) by a motor-driven pulley-cord-system activating a panel attached to a piston moving through the tank beneath the plexiglass layer. In each experiment, two silicone plates representing a subducting oceanic plate and an overriding continental plate are placed on top of the mantle. We simulate three scenarios (Figure 1): a) no mantle flow (slab-pull driven subduction, model 1), b) mantle flow directed toward the overriding plate (models 2, 4 and 5), and c) mantle flow directed toward the subducting plate (model 3). Either the overriding plate or the subducting plate is fixed to a back wall to avoid a global drift of the system.

We use glucose syrup (Cargill 01497) as an analogue material for the sub-lithospheric mantle. The syrup has the consistency of honey and can be considered as a Newtonian fluid since its viscosity is not sensitive to shear rate. In contrast, it varies strongly as an inverse function of temperature (e.g., *Schellart*, 2011). During our experimental campaign, the temperature of the syrup varied between 19.1–19.9°C, corresponding to a range of viscosities of ~177–209 Pa.s, as calculated from a Couette viscometer at the Géosciences Rennes (France) laboratory. Uncertainty on viscosity measurements is ±10 Pa.s. The density of the glucose syrup is considered constant in the recorded temperature range, and has been determined at 1420 ± 5 $kg.m^{-3}$ (Table 1).

The lithospheric plates are modeled as viscous layers made of silicone putties. The viscosity of silicones can be considered constant in the range of temperatures recorded in the laboratory and as independent of the shear rate for values lower than 0.5 s^{-1} (e.g., *Rudolf et al.*, 2016). Given that strain rates in the models are much lower than that, silicone can be considered as a Newtonian material in our experimental conditions. Three different silicones have been used to model the oceanic and continental plates. For the oceanic lithosphere, we used a transparent PDMS silicone (density of 965 $kg.m^{-3}$) filled with iron powder to increase its density to 1480 ± 5 $kg.m^{-3}$, which corresponds to a negative buoyancy of -60 ± 10 $kg.m^{-3}$ with respect to the syrup. Viscosities were measured with a Haake rheometer at IPGP (France) from oscillatory tests (e.g., *Habel*, 2022). The oceanic plate has a viscosity of ~99800 Pa.s and a thickness of 14 ± 0.2 mm (Table 1). This corresponds to a slab-to-mantle viscosity contrast ranging between 478 and 564 (Table 1). To model a strong continental lithosphere, we used the same silicone but with a lower density (1297 ± 5 $kg.m^{-3}$), a slightly lower viscosity of ~90000 Pa.s, and a thickness of 8 ± 0.2 mm. To model a weaker continental lithosphere, we used orange silicone, with a significantly lower viscosity of ~14600 Pa.s (~16% of the stronger lithosphere's viscosity), but slightly higher density of 1327 ± 5 $kg.m^{-3}$, and the same thickness (Table 1). It corresponds to a positive buoyancy of +93 ± 10 $kg.m^{-3}$ for the weaker silicone, and +123 ± 10 $kg.m^{-3}$ for the stronger one, compared to the syrup.

2.2 Scaling laws

The experiments are properly scaled for gravity, length, density, viscosity, and velocity following the method of previous studies (e.g., *Guillaume et al.*, 2021). The length scaling factor between model and nature is 1.52×10^{-7}, meaning that 1 cm in the model corresponds to 66 km in nature (Table 1). The trench-parallel width (hereafter "width") of both oceanic and continental plates is ~30 cm in the laboratory (Figure 1), thus scaling to ~1980 km in nature, a value comparable to the Central Andean segment along the Chilean coast from ~17°S to ~35°S. The initial trench-orthogonal length (hereafter "length") is ~30 cm for the overriding plate and ~40 cm for the subducting plate (Figure 1), i.e., ~2640 km for the latter at Earth's scale. The widths and lengths varied at most by ± 0.8 cm due to manual preparation and minor deformation when placing the plates over the syrup. The thicknesses of ~1.4 cm and ~0.8 cm of the analogue oceanic and continental lithospheric plates correspond to ~92 km and ~53 km in nature, respectively. The

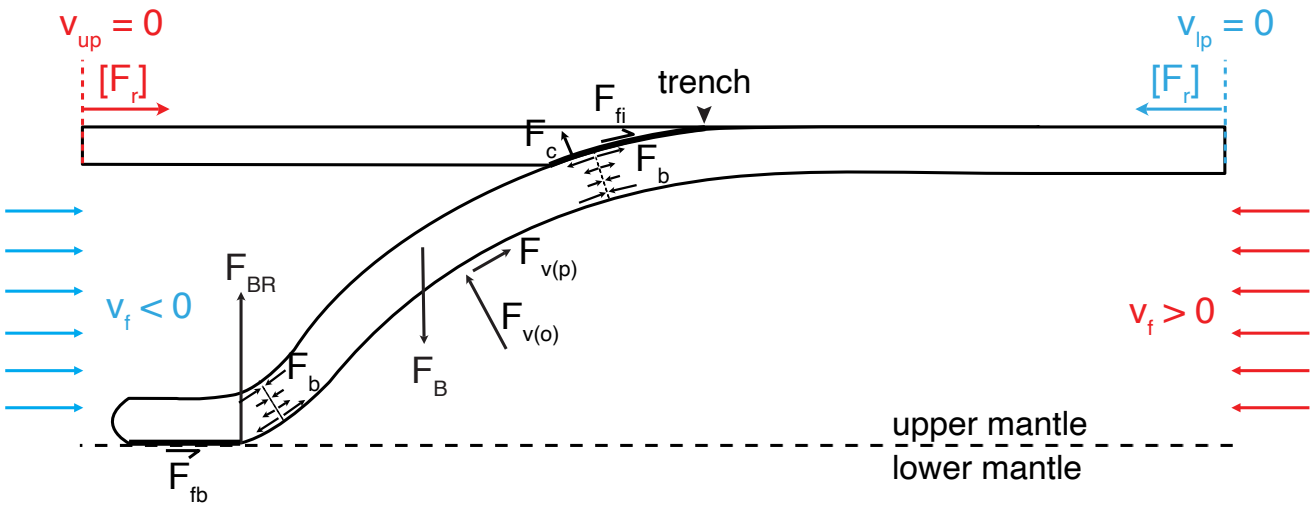

Figure 2 – Sketch showing the different forces at work and the kinematic boundary conditions in a vertical plane of our experimental subduction system. Abbreviations: F_B: slab pull force; F_r: back wall reaction force; F_b: slab bending force; F_v: viscous forces in the mantle orthogonal to the slab ($F_{v(o)}$) and parallel to the slab ($F_{v(p)}$); F_{fi}: friction at the plates interface; F_{fb}: friction at the interface between the slab and the bottom of the box; F_{BR}: basal resistance of the bottom of the box; F_c: force transmitted to the upper plate; V_{up}: upper plate velocity; V_{lp}: lower plate velocity; V_f: mantle flow velocity. We recall that this 2D sketch is only schematic of our 3D models, in particular for the representation of viscous force F_v.

thickness of the oceanic plate would correspond to a 50 Ma old oceanic lithosphere according to the oceanic lithosphere half-space cooling model (e.g., *Turcotte and Schubert*, 2002), which is close to the average age of the oceanic crust at trench along the South America subduction zone during the Cenozoic (e.g., *Müller et al.*, 2016). The chosen value for the initial overriding continental plate thickness may be considered as low, but it allows us to better observe and quantify deformation in our experiments, as the amount of deformation scales with thickness in our viscous models. As such, obtained amounts and rates of deformation may be seen as an upper bound.

The time scaling factor is calculated from the syrup/mantle viscosity contrast between model and nature, depending on measured syrup temperature in the model, from the density contrast between the oceanic plate and the mantle, and from the thickness of the slab (e.g., *Davy and Cobbold*, 1991; *Martinod et al.*, 2005; *Armijo et al.*, 2015). The sub-lithospheric mantle viscosity in nature is loosely estimated between 10^{19}–10^{21} Pa.s depending on depth (e.g., *Mitrovica and Forte*, 2004). When assuming an average value of 5×10^{20} Pa.s, we obtain a time scaling where 1 Myr in nature scales to ~74–87 s in the models (Table 1), given the range of measured syrup temperatures.

When activated, the mantle flow velocity (~630–740 mm.h^{-1} in the lab, for the laboratory temperature range) is scaled to represent 10 cm.yr^{-1} in nature. We chose this background flow velocity to be faster than the subduction velocity in the absence of mantle flow (82 mm.h^{-1}, corresponding to 1.2 cm.yr^{-1}in nature, on average, as measured in model 1) in order to be in the experimental conditions where the mantle can drag the free plate. Additionally, such fast mantle flow is found to be needed to experimentally generate reasonable scaled subduction and convergence rates of a few cm/yr, as observed in nature.

2.3 Forces equilibrium

Orogenic growth is controlled by the equilibrium between boundary and buoyancy forces (e.g., *England and McKenzie*, 1982; *Conrad and Hager*, 1999). Boundary forces allow for building up topography, while buoyancy forces are the ones opposed to orogeny. In the case of topographic building in a subduction context, the boundary forces leading to shortening of the continental lithosphere are largely dependent on the forces controlling the subducting system (Figure 2). The driving force that is common to all models is the negative buoyancy force of the oceanic slab (F_B), depending on the plate-to-mantle density contrast and on the volume of the slab. Resistive forces in the system evolve over time and include (a) resistance to slab bending (F_b) when plunging into the mantle and when touching the lower discontinuity, depending mainly on the radius of curvature of the bending slab, on the slab's effective viscosity and on the subduction velocity (e.g., *Buffett*, 2006), (b) friction forces between the slab and the lower discontinuity after the slab interacts with the upper-lower mantle interface (F_{fb}), (c) basal force exerted by the lower discontinuity that resists slab vertical sinking (F_{BR}), (d) viscous forces exerted by the mantle resisting slab roll-back ($F_{v(o)}$) and sinking ($F_{v(p)}$). Activation of a background mantle flow may turn the viscous forces into a driving force under certain conditions, promoting plate displacement and subduction by mantle drag at the base of the lithosphere.

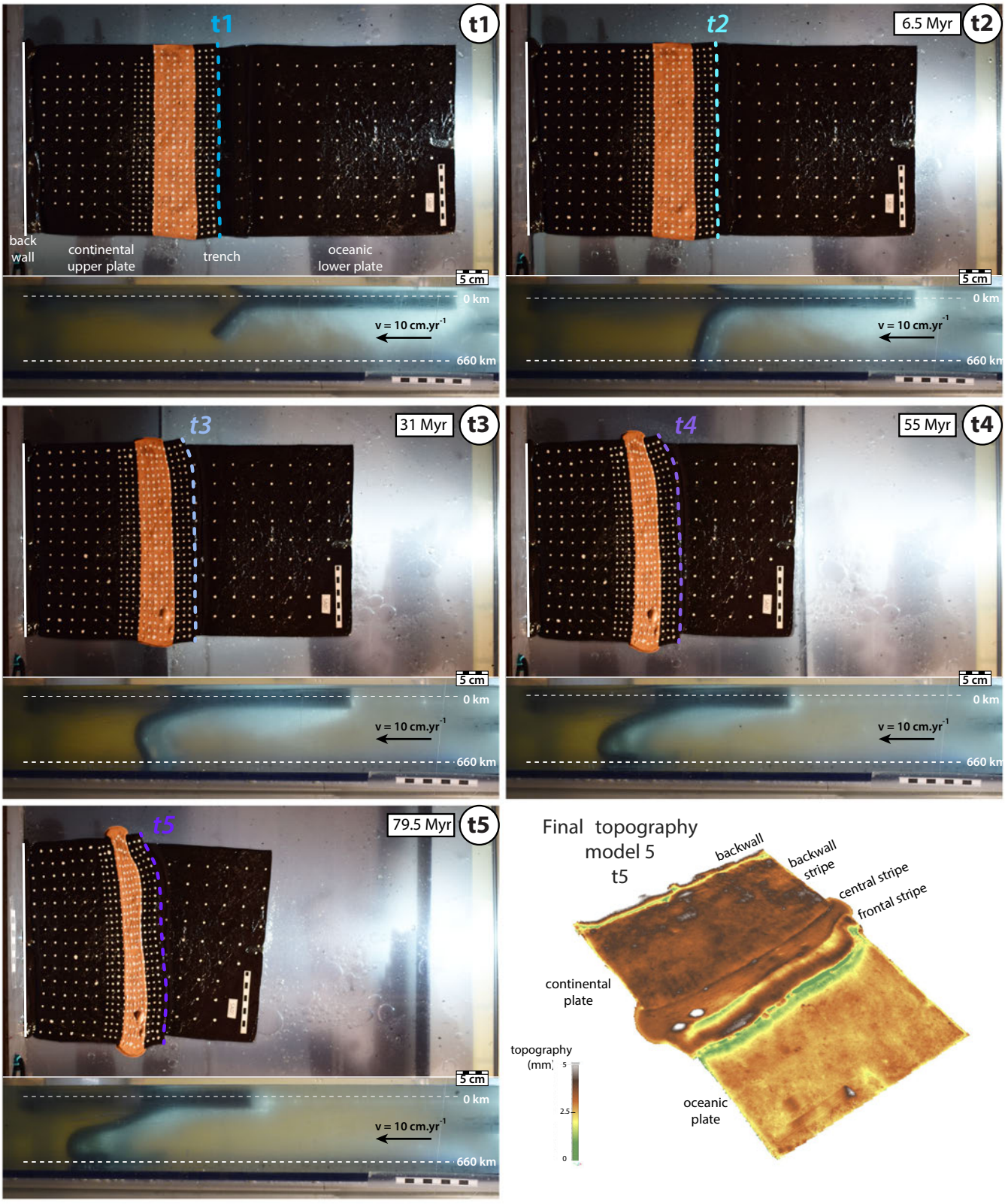

Figure 3 – Top and lateral views of the different stages (t1 to t5) for experiment model 5. t1: onset of subduction; t2: slab arrival at the bottom of the box (analogue of an impermeable upper-lower mantle discontinuity); t3 and t4: evolution of the slab geometry after interacting with the discontinuity at the base of the flowing mantle; t5: end of the experiment. Oblique view of the final surface topography at t5.

The inclusion of an overriding plate in the system adds other resisting forces like friction at the interface between the oceanic and continental plates (F_{fi}), which is limited here by using a mix of vaseline and paraffin oil at the plates' interface (e.g., *Duarte et al.*, 2014, 2015; *Zhong and Gurnis*, 1994). Part of the force driving the subduction is transmitted at the plate interface onto the overriding plate (F_c) by the advancing trench, and contributes to deforming the upper plate.

By fixing one of the two plates (either the oceanic or the continental plate) to a back wall, we impose a no-motion boundary condition, generating a reaction force perpendicular to the wall (Fr). For models with flow directed toward the lower plate, this force constantly adjusts to balance the trenchward force that applies to the plate, making Fr a resisting force (blue case in Figure 2). For models with flow directed toward the upper plate, Fr prevents the upper plate from moving away from the trench, increasing coupling between plates, and as such should be considered also as a resisting force (red case in Figure 2).

In our experimental set-up, as in published ones (e.g., *Guillaume et al.*, 2021), the leading edge of the oceanic plate is initially forced downward into the syrup to a depth of 2-3 cm. The mechanisms and forces initiating the plunging of the oceanic lithosphere are therefore beyond the scope of this work.

2.4 Measurements, uncertainties, and limitations

High-resolution top and lateral photos have been taken every minute during the entire experiment with a DSLR camera (Nikon D-3200) with a resolution of 6000x4000 pixels. These photos have then been analyzed to measure (a) the velocity of the free plate, i.e., the overriding plate in model 3 and the subducting plate in the other models, (b) the amount of upper plate horizontal deformation in the direction parallel to the flow measured in the center of the plate, (c) the amount of upper plate thickness change as quantified by the variations in upper plate area (as material is incompressible), and (d) the dip of the slab measured on the side view at a depth of 2.3 cm in the experimental set-up (equivalent to ~150 km in nature). To further monitor the evolution of deformation within the overriding plate, a grid pattern of white dots has been initially drawn on the silicone putties, spaced by 2 cm or 1 cm in some strips for a higher resolution where deformation is more intense (Figure 3). The displacement field obtained from the digitization of the dots is then processed with the SSPX software (e.g., *Cardozo and Allmendinger*, 2009) to compute rates of horizontal shortening (strain rates for the minimum principal axis of the horizontal strain ellipse). For one experiment (model 5), we collected 42 pictures taken at different angles for the final stage of the experiment that were processed using the Agisoft Metashape program to obtain a Digital Elevation Model of the surface (Figure 3).

The uncertainty related to our measurements is minor and generally within the thickness of the drawing when graphically represented. The scaled velocity values are obtained for each model by applying a proper velocity factor (Table 1). The estimated uncertainty on measuring the slab dip is of ±3°. This angle was monitored only on the one side of the experimental box equipped with cameras, which could be a limitation in some experiments where the geometry of the slab is not perfectly cylindrical.

Laboratory experiments have unavoidable limitations, first by being isothermal, thus neglecting phase changes, thermal conduction and diffusion (e.g., *Funiciello et al.*, 2003; *Guillaume et al.*, 2021). Also, the plates are modeled as vertically homogeneous plates with viscous rheology, therefore not taking into account brittle deformation that could develop in the crust and/or mantle. The rigid interface simulating the upper–lower mantle transition constitutes an impermeable barrier, rendering slab penetration impossible in the lower mantle, and therefore possibly overestimating forces exerted by this interface on the subduction system. Finally, the mantle is assumed here to behave as a Newtonian fluid, which implies that deformation may be more diffuse when comparing it to a mantle behaving as a power-law fluid (e.g., *Brace and Kohlstedt*, 1980; *Ranalli*, 1995).

3 Results

Five experiments have been performed to test the role of the mantle flow direction and the effect of plate strength on the deformation regime of the continental upper plate (Figure 1). In model 1, the background mantle flow is absent, the overriding plate is fixed to the back wall, and the subducting plate is free to move under the pull exerted by the sinking part of the subducting plate. In model 2, the imposed background flow drives the lower oceanic plate against the upper continental plate. In model 3, we tested the opposite plate configuration: the oceanic plate is fixed to the back wall, and the continental plate is free and driven by the mantle flow directed toward the oceanic plate. Then, in order to explore the role of the upper plate's structure for its subsequent deformation in a subduction context equivalent to model 2, we placed pre-existing heterogeneities in the upper plate by positioning either one central stripe of weaker lithosphere in the upper continental plate (model 5) or two weaker stripes, one located close to the trench and the other close to the back wall (model 4). During the experiment, t0 represents the initial stage (before initiation of the subduction, 0 minute), t1 the onset of subduction, t2 the moment when the slab touches the upper-lower mantle discontinuity, and t5 the end of the experiment (Figure 3). Additional intermediate stages t3 and t4 illustrate the evolution of the slab geometry after interacting with the upper-lower mantle discontinuity, as shown on the top and lateral snapshots of each stage for model 5 (Figure 3). Given that the time scaling is slightly different for each experiment because of small variations in syrup temperature (and viscosity), we report time, distances, and velocities using the equivalent values in nature (see Table 1 for scaling) to more easily compare the experiments.

Model				model1	model2	model3	model4	model5	Nature
Laboratory name				(SA03)	(SA02)	(SA01)	(SA04)	(SA05)	
	Parameter	Symbol	Unit						
Oceanic plate	thickness	h	mm	14±0.2	14±0.2	14±0.2	14±0.2	14±0.2	92.4x10^6
	density	ρ_{op}	kg.m^{-3}	1480±5	1480±5	1480±5	1480±5	1480±5	
	buoyancy	$\triangle\rho$	kg.m^{-3}	60	60	60	60	60	60
	viscosity	η	Pa.s	99800	99800	99800	99800	99800	2.4-2.8x10^{23}
Strong continental plate	thickness	h	mm	8±0.2	8±0.2	8±0.2	8±0.2	8±0.2	52.8x10^6
	density	ρ	kg.m^{-3}	1297±5	1297±5	1297±5	1297±5	1297±5	
	viscosity	η	Pa.s	90000	90000	90000	90000	90000	2.15-2.5x10^{23}
Weak continental plate	thickness	h	mm				8±0.2	8±0.2	52.8x10^6
	density	ρ	kg.m^{-3}				1327±5	1327±5	
	viscosity	η	Pa.s				14600	14600	3.5-4.1x10^{22}
Sub-lithospheric mantle	thickness	h	mm	100±0.2	100±0.2	100±0.2	100±0.2	100±0.2	660x10^6
	density	ρ_m	kg.m^{-3}	1420±5	1420±5	1420±5	1420±5	1420±5	
	viscosity	η	Pa.s	189	209	193	185	177	5x10^{20}
Boundary conditions	mantle velocity fixed plate	v_f	mm.h^{-1}	- upper	625 upper	-680 upper	709 upper	739 upper	
Scaling	length (1 km)		mm	0.15	0.15	0.15	0.15	0.15	
	$t_{Nature}/t_{model} = (\triangle\rho g h)_{model}/(\triangle\rho g h)_{Nature}\cdot(\eta_{Nature}/\eta_{model})$								
	time (1 Ma)		s	79	87	80	77	74	
	$v_{Nature}/v_{model} = (L_{Nature}\cdot t_{model})/(L_{model}\cdot L_{Nature})$								
	velocity (10 cm.yr^{-1})		mm.h^{-1}	696	625	680	709	739	

Table 1 – Properties of analogue materials. Viscosities are given for measurements made at strain rates of 0.01 s^{-1}, and for measured syrup temperatures (19.1–19.9°C) in the case of the viscosity of the sub-lithospheric mantle. Positive values for mantle flow velocities correspond to a flow directed toward the upper plate. Scaling for length, time, and velocities are given considering a sub-lithospheric upper mantle viscosity of 5×10^{20} Pa.s in nature. The models have been renamed (models 1 to 5) from the initial names in the laboratory (SA01 to 05) for an easier reading, and the correspondence between the two labelings is given in this table

3.1 Slab pull-driven subduction

When mantle flow is absent (model 1), the subducting plate is free to sink under its own weight while the overriding plate is fixed to the back wall (Figure 1). Within these boundary conditions, oceanic slab roll-back is observed, inducing an important trench retreat that ultimately leads to the opening of a gap between the two plates, filled with upwelling sub-lithospheric mantle (Figure 4). The upper continental plate initially deforms by trench-orthogonal horizontal stretching but at a rate that is not as fast as the rate of trench retreat. During the experiment, the slab touches the mantle discontinuity after ~7.6 Myr (t2, 10 minutes in the lab), and the final stage (t5) is after ~36.4 Myr (48 minutes). The slab-dip at 150 km depth increases up to 45° until the slab reaches the 660 km discontinuity (Figure 5). It then stabilizes at values around 40°. After subduction initiation, the trench retreats toward the subducting plate by ~224 km (3.4 cm) after 36.4 Myr, i.e., at an average retreat rate of ~0.6 cm.yr^{-1}. At the same time, we observe a trench-orthogonal horizontal stretching of the continental plate of ~73 km (1.1 cm in the lab) for an initial length of ~1993 km (30.2 cm), i.e., 3.6% of stretching (Figure 5). This modeled upper-plate extension recalls back-arc extension and basin opening often observed in natural subduction contexts affected by slab roll-back (e.g., Sumatra, Mariana). However, the amount of modeled extension cannot be directly compared to natural observations because it is limited in the model by the chosen boundary conditions (fixed upper plate) and the mechanical property of the silicone plate. Finally, we note that in the absence of a fixed velocity condition for the continental plate (i.e., detached from the back wall), the entire upper plate would have probably followed the retreating trench, associated with limited (or even no) stretching (e.g., *Schellart et al.*, 2007; *Schellart*, 2017; *Guillaume et al.*, 2018).

3.2 Mantle-driven subduction

In model 2, the continental plate is fixed to the back wall, and the oceanic plate moves toward the continent driven by both the underlying imposed mantle flow at 10 cm.yr^{-1} and its own weight (Figure 1). On the side view, the oceanic plate keeps a moderate dip angle in the upper mantle and flattens at depth after reaching the mantle discontinuity after 13.1 Myr (t2) (Figure 4). At 150 km depth, the slab dip angle progressively increases from 19° (t1) to 38° during the first 5 Myr. Then, subduction continues without a slab dip increase until after 35 Myr. Afterwards, the slab dip progressively increases up to 51° at the end of the experiment (70.3 Myr) (Figure 5). The oceanic plate moves rapidly at ~8 cm.yr^{-1} during the first 6 Myr, and slows down progressively to reach a value of ~1.2 cm.yr^{-1} after 20 Myr, i.e., 12% of the imposed underlying mantle velocity, which then remains almost constant until the end of the experiment (Figure 5). This leads to a total of ~548 km (8.3 cm) of subducted plate, i.e. an average rate of ~0.8 cm.yr^{-1} (Figure 4). The trench progressively advances towards the upper continental plate, which in turn undergoes flow-parallel shortening and thickening. The upper plate shortening in the center of the plate reaches a final amount of 22%, with an average strain rate (0.31x10^{-2} Myr^{-1}). Deformation

appears almost homogeneous at the scale of the plate during the entire duration of the experiment (Figure 5). The evolution of upper plate thickening is comparable to that of shortening, with a calculated final amount of 16%, indicating that flow-orthogonal horizontal stretching occurred but at a slower rate than flow-parallel shortening.

In contrast in model 3, the oceanic plate sinks into the mantle under its own weight, and we impose a background mantle flow directed toward the subducting plate at a velocity of 10 cm.yr^{-1}, resulting in the displacement of the upper continental plate toward the subducting oceanic slab (Figure 1). On the side view, we observe that the slab progressively steepens, before folding forward after it reaches the mantle discontinuity after 15 Myr (t2) (Figure 4). The slab dip at 150 km depth steepens rapidly from 39° (t1) to 52° (t2), and increases only slightly afterwards up to 60° after 45-48 Myr, to finally decrease to 53° at the end of the experiment (t5, 55.5 Myr) (Figure 5). The trench retreats toward the subducting plate rapidly at the beginning (t1–t3, during 28.5 Myr), whereas its position remains overall steady after 42 Myr (t4). The length of the oceanic slab (amount of subducted lithosphere) increases rapidly at the beginning until it reaches the mantle discontinuity (t2), but nearly no more afterwards. The final amount of subducted plate raises ~389 km (5.9 cm in the lab), giving an average rate of ~0.7 cm.yr^{-1} for the duration of the experiment, comparable to model 2 (Figure 4). The continental lithosphere shows an initial plate displacement toward the subducting plate of up to ~6 cm.yr^{-1} that decreases to ~1.5 cm.yr^{-1} before the slab reaches the mantle discontinuity. After slab anchoring, the upper plate continues to move in the direction of the imposed mantle flow with an average rate of 0.5 cm.yr^{-1}. The length of the upper plate parallel to the mantle flow, as measured in its central part, decreases over the whole experiment, from ~1973 km at t1 (29.9 cm) to a final value of ~1861 km at t5 (28.2cm), corresponding to a total amount of shortening of 5.7% (Figure 5), with an average strain rate of 0.1x10^{-2} Myr^{-1}), around 3 times slower than in model 2. Although flow-parallel shortening is recorded in the center of the upper plate, the entire upper plate is thinned by 3.8% at the end of the experiment, indicating a larger horizontal stretching of the upper plate in the flow-orthogonal direction.

Altogether, these first three experiments provide key insights into the conditions needed to generate shortening in the upper plate of a subduction zone. Subduction only driven by the negative buoyancy of the slab (model 1) leads to trench-orthogonal horizontal stretching of the fixed upper plate (Figure 5). In contrast, shortening of the continental upper plate is produced in both models 2 and 3 where either the lower or the upper plate is additionally dragged toward the trench by an imposed mantle flow, and the other plate is fixed. Mantle tractions resulting from the imposed background flow therefore appear as an essential force not only to drive the subduction process, but also to trigger shortening and possibly thickening of the continental lithosphere. The free plate is driven by the mantle flow toward the plate fixed to the back wall, resulting in net trench displacement, mostly trench advance in the case of model 2 or trench retreat/stagnation in the case of model 3. At the plate's interface, this generates a force that is transmitted to the upper continental plate (Figure 2). This latter absorbs the convergence by trench-orthogonal shortening resulting in thickening and/or widening on the free side edges. Additionally, the chosen boundary conditions (direction of mantle flow with respect to subduction, which plate is fixed to the back wall) have a profound effect on how much the upper plate deforms. Imposing a no-velocity condition for the overriding continental plate by fixing it to the back wall (model 2) results in net trench advance and in mean strain rates of 0.31x10^{-2} Myr^{-1} for the horizontal shortening and 0.23x10^{-2} Myr^{-1} for the vertical deformation, which are much higher and significant than the 0.1x10^{-2} Myr^{-1} for shortening and 0.07x10^{-2} Myr^{-1} for thinning measured when the subducting oceanic plate is fixed to the back wall (model 3) (Figure 5). In both experiments, the slab geometry is very different, with a slab folding forward in the case of mantle flow directed toward the lower plate (model 3), versus a slab down-laying at depth for a mantle flow directed toward the upper plate (model 2) (Figure 4).

3.3 Pre-existing heterogeneities within the overriding plate

In the following models 4 and 5, we aim at investigating how the distribution of deformation within the overriding plate is influenced by its pre-existing structuring and strength distribution (Figure 6). We use here the same configuration as for model 2: the overriding continental plate is fixed to the back wall and the subducting oceanic plate is freely moving over the imposed underlying mantle flow (V_f= 10 cm.yr^{-1}), thus reproducing the boundary conditions favoring maximum upper-plate shortening. We introduce stripes of weaker lithosphere (orange) , whose viscosity corresponds to ~16% of that of the stronger lithosphere. In the case of model 4, the upper plate is divided into three 660 km (10 cm) long stripes parallel to the trench, the central one being made of stronger silicone (black), and the two other ones of weaker silicone (weaker silicone representing ~67% of the total volume of the plate). In the case of model 5 the weaker silicone stripe is incorporated within the stronger upper plate (weaker silicone representing 20% of the total volume of the plate). The weaker silicone, which is 396 km (6 cm) long, is placed at a distance of 264 km (4 cm) from the trench in model 5. The continental lithosphere of model 4 therefore has an average viscosity corresponding to ~53% of that of model 5.

In both experiments, the slab arrives at the mantle

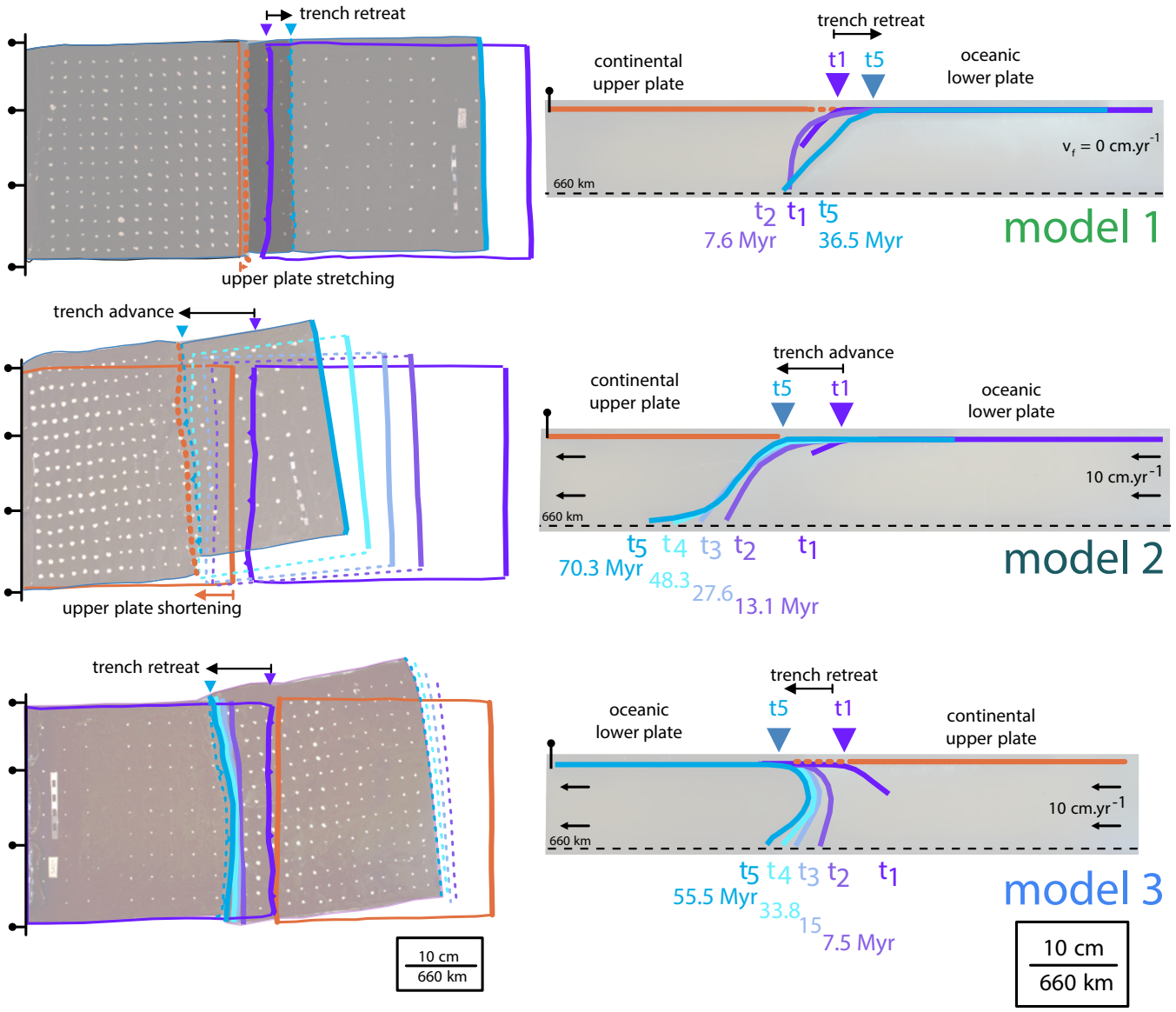

Figure 4 – Top and lateral views of models 1, 2 and 3. Position of the free plate trailing edge (solid lines on top views), trenchward upper plate edge (dashed lines on top views), and slab shape (solid lines on lateral views) are indicated at five different times (t1 to t5). Position of the trench at the beginning (t1) and at the end (t5) of the experiment is indicated by a solid line with triangles on top views.

discontinuity after ~6 Myr, then folds forward until the end of both experiments after ~65 Myr for model 4 and ~79 Myr for model 5 (Figure 3 and 6). At 150 km depth, the slab steepens rapidly until it reaches the mantle discontinuity with values up to 51° for model 4 and 58° for model 5. Then, the slab dip decreases to reach values of 25° after 20 Myr for model 4 and 30 Myr for model 5 (Figure 5). For model 5, the slab dip increases by 8° during the last 20 Myr. For model 4, the slab shape does not evolve symmetrically, one edge deforms as in model 2 (slab down-laying), not imaged by our side-view snapshots taken from the other side only, where the slab folds forward as in model 5 (Figure 6). This illustrates the fact that the shape of the slab is not dependent only on the mantle flow direction. The oceanic plate subducts rapidly before the slab reaches the mantle discontinuity, and slows down progressively afterwards. For model 4, the final subducted length varies along-width between 1056 km (16 cm) and 1584 km (24 cm), and for model 5 it varies between ~977 km (14.8 cm) and ~1241 km (18.8 cm), giving average subduction velocities of 1.6 to 2.4 cm.yr^{-1} for model 4, and 1.2 to 1.6 cm.yr^{-1} for model 5, faster than in model 2 (0.8 cm.yr^{-1}) (Figure 6). The evolution of the oceanic plate velocity appears almost identical to that of model 2 with a first phase of trenchward motion with velocities up to ~8 cm.yr^{-1} (model 5) and ~10 cm.yr^{-1} (model 4), which rapidly decrease once the slab has reached the mantle discontinuity. Afterwards, the plate velocity remains almost constant with mean values of 1.3 cm.yr^{-1} and 2 cm.yr^{-1} for models 4 and 5, respectively (Figure 5).

The center of the continental plate records a total of 31% of trench-orthogonal shortening in model 4 after 65 Myr, giving a mean strain rate of 0.48x10^{-2}

Myr^{-1}, ~50% faster than the mean strain rate in model 2 (Figure 7). For model 5 it is $0.37x10^{-2}$ Myr^{-1}, ~20% faster than for model 2. For both models 4 and 5, the upper plate thickens with vertical deformation rates of $0.34x10^{-2}$ $Myr^{-1}$for model 4 and $0.31x10^{-2}$ Myr^{-1} for model 5 (Figure 5 and 7). In both experiments, deformation is preferentially localized in the weak silicone, whereas the more viscous silicone behaves as a relatively more rigid block (Figure 7). Furthermore, blocks with the same viscosity deform more significantly when they are close to the back wall than when they are close to the trench with differences of up to 50% on the mean deformation rate for model 5. Upper plate flow-orthogonal stretching is also more important for the weaker silicone, as illustrated on the final top view of both experiments (Figure 6). Furthermore, for model 5, the weak silicone is uplifted compared to the strong one, and rolls over it (Figure 3). Bulk finite upper plate shortening and thickening rates are the highest in model 4, where the continental plate is on average the weakest (Figure 7B). However, the difference in thickening rate is not as important as the difference in shortening rate, indicating an overall larger flow-orthogonal stretching in model 4, owing to the overall lower strength of the upper plate (Figure 5). As a conclusion, models 4 and 5 illustrate how lateral variations in overriding plate strength resulting from pre-existing structuring can control the distribution of deformation once the conditions are met to generate compression within the upper plate.

4 Discussion

4.1 Conditions promoting shortening of the upper continental plate in an oceanic subduction context

Our models aim at reproducing in three dimensions the subduction of an oceanic slab under an upper continental plate and at testing the boundary conditions that favor upper plate shortening. Interestingly, plate displacement is here not only controlled by slab pull but also by mantle drag at the lithosphere-asthenosphere boundary, allowing plate velocity adjustments according to the balance of forces in the system (Figure 2).

One of the main experimental limitations lies in the fact that our models do not explicitly reproduce slab anchoring at the discontinuity between the upper and lower mantle, which is here considered impermeable (Figure 1). This impedes slab penetration into the lower mantle and in turn, results in slab tip horizontal motion at the base of the model under the imposed mantle flow (toward the lower plate for model 3, and toward the upper plate for models 2, 4 and 5) (Figure 4 and 6). Previous studies have proposed that penetration of the slab into the lower mantle limits trench mobility and triggers whole mantle convection, resulting in accelerated mantle flow under the plates, and upper plate change in deformation regime from extension or mild shortening to significant shortening (e.g., *Quinteros and Sobolev*, 2013; *Schellart*, 2017; *Faccenna et al.*, 2017; *Chen et al.*, 2019). We therefore cannot directly compare our results with these previous studies because here mantle flow is imposed and maintained constant throughout the entire experiment. However, our results clearly indicate that mantle flow is fundamental, as the comparison between models with and without mantle flow suggests that an increase in mantle flow beneath the plates could possibly induce larger shortening.

The possibility to add mantle flow in our experiments to understand its impact on subduction dynamics and on the tectonics of the upper plate is one of the main merits of our set-up. However, mantle flow and associated mantle drag are here only unidirectional and cannot strictly reproduce more complex scenarios where mantle drag is opposite on both sides of the subduction, as could be the case for some of the current subduction zones such as in the Andes (e.g., *Husson*, 2012). We recall here that even though unidirectional flow drags one of the plates, the other one is fixed and as such undergoes a reaction force Fr from the back wall that impedes its mobility, which can be taken for the equivalent of a force driving this plate toward the trench (Figure 2). Our setting cannot therefore be directly compared to modeling results where both plates are set free (e.g., *Capitanio et al.*, 2011; *Schellart and Moresi*, 2013; *Holt et al.*, 2015), but it is worth noticing that in those models shortening is favored when the trench is almost stationary and when poloidal flow induced by subduction is vigorous enough to generate tractions at the base of the lithosphere, driving the upper plate toward the trench. These studies therefore underline the importance of poloidal flow and mantle drag in controlling the tectonic regime of the overriding plate. Our models, in which mantle flow is not only driven by slab pull, consider that subduction zones are not isolated systems, and as such may be more realistic.

Despite these limitations, our original experiments provide key insights into the conditions that are expected to promote upper plate shortening in an oceanic subduction context. In more detail, our experiments show that where plate convergence is not only driven by slab pull but also by a background mantle flow dragging the subducting plate or the upper plate toward the trench while the other plate is fixed, the continental plate deforms with significant shortening and, in some cases, thickening (Figure 5). We further identify two main factors promoting shortening and thickening. The first factor is the direction of the imposed mantle flow, combined with a no-velocity condition applied to the overriding plate (Figure 4). A mantle flow toward the continental plate attached to the back wall acting as a buttress enhances shortening, with more shortening in models 2, 4 and 5 than in model 3 (Figure 5).

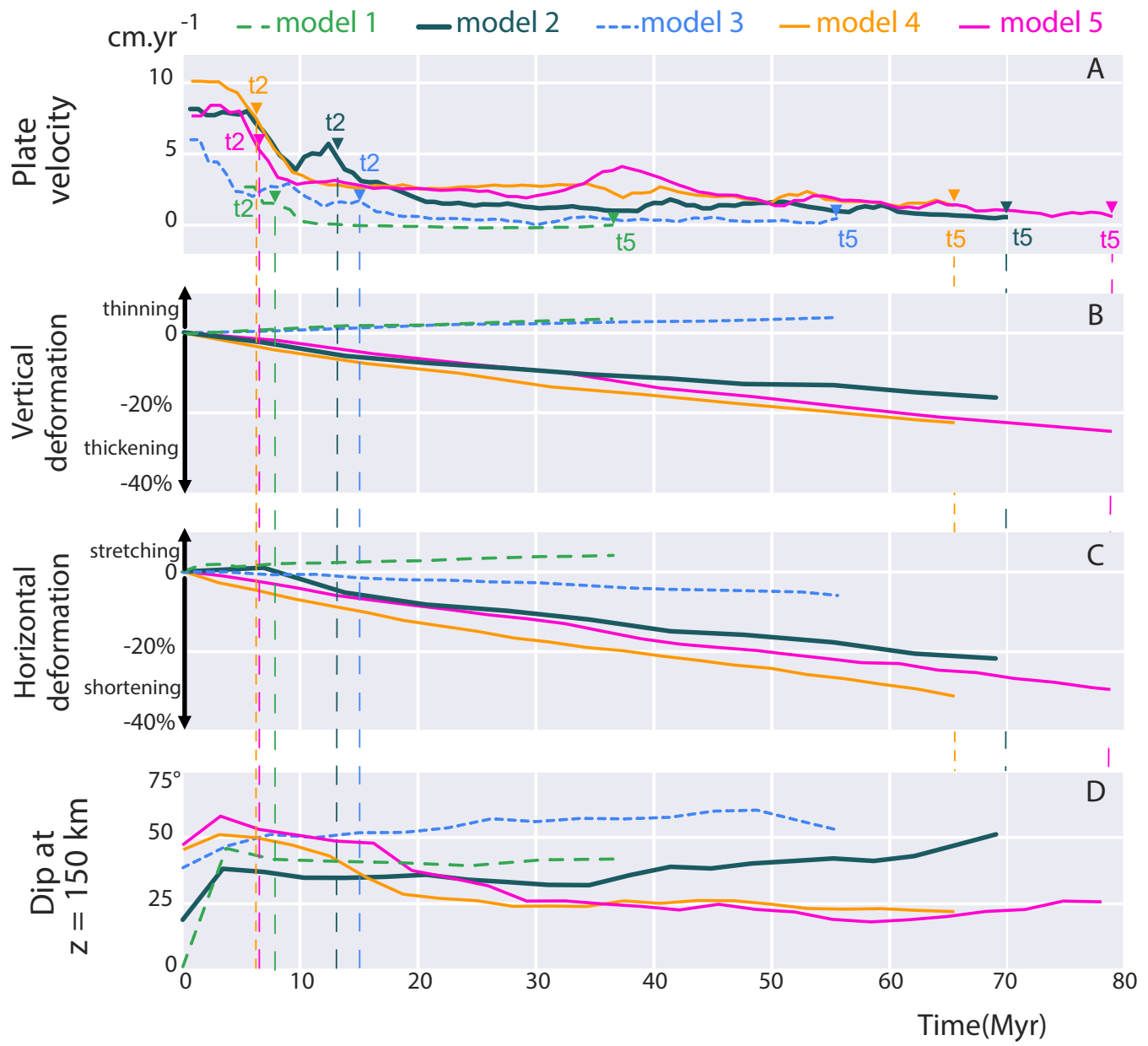

Figure 5 – **(A)** Plate velocity for the free plate in models 1 to 5 (oceanic plate in all cases, except for model 3). Triangles at t2 indicate the time when the slab reaches the bottom of the box (660 km depth discontinuity), and triangles at t5 indicate the end of the experiments. **(B)** Cumulative amount of upper plate vertical deformation, in %. Thickening corresponds to negative values. **(C)** Cumulative amount of upper plate flow-parallel shortening/stretching, in %, measured in the center of the plate. Shortening corresponds to negative values. D) Slab dip angle measured at 150 km (2.3 cm) depth.

These boundary conditions induce a significant net trench advance, as the drag of the oceanic plate toward the upper plate by the underlying mantle flow exceeds the average velocity of slab retreat. Accordingly, absolute plate velocities are modified, and the upper lithosphere is put under compression. Such net trench advance, when the forward motion of the upper plate is faster than the backward motion of the trench, has already been pointed out as a main mechanism for building an orogenic range in an oceanic subduction context in several numerical and analogue models (e.g., *Sobolev and Babeyko*, 2005; *Schellart et al.*, 2007; *Capitanio et al.*, 2011; *Schellart*, 2008, 2017; *Cerpa et al.*, 2018; *Guillaume et al.*, 2018; *Wolf and Huismans*, 2019). Second, the bulk strength of the upper plate is also a key factor controlling the amount of accommodated shortening in the upper plate, in line with published work (e.g., *Wolf and Huismans*, 2019): more shortening is obtained in model 4 than in model 5, which in turn records more shortening than in model 2, as the bulk strength of the continental plate decreases (Figure 5 and 7). A pre-existing structuring of the upper continental plate is a requisite to strongly localize the deformation. As plates are modeled here with viscous materials with a Newtonian behavior at low strain rate, the upper plate pre-structuring with blocks of different viscosities promotes deformation localization in the weaker (orange) silicone compared to the stronger (black) one (Figure 7).

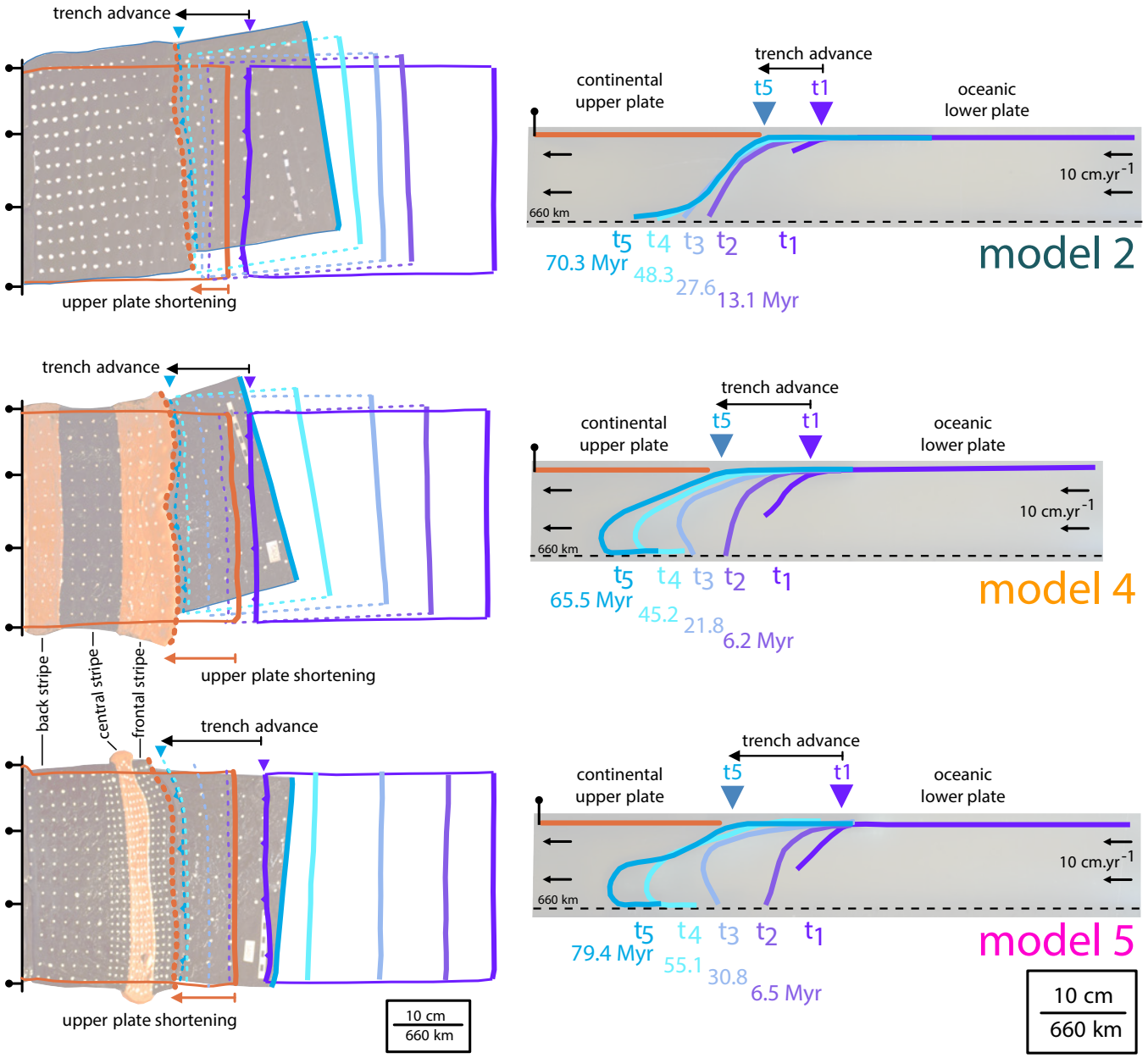

Figure 6 – Top and lateral views of models 2, 4 and 5. Position of the free plate trailing edge (solid lines on top views), trenchward upper plate edge (dashed lines on top views), and slab shape (solid lines on lateral views) are indicated at five different times (t1 to t5). Position of the trench at the beginning (t1) and at the end (t5) of the experiment is indicated by a solid line with triangles on top views.

Additionally, even though we are not able to experimentally reproduce flat slabs stricto sensu (i.e., nearly horizontal slabs at the base of the upper-plate crust like in Mexico or at the base of the lithosphere, like in Peru and Chile), our models allow for discussing slab geometries and their proposed impact on upper plate shortening. We observe that the slab is either rolling over with a relatively flat slab segment below the overriding plate (model 5 - with stronger shortening), or flatly lying at the transition between the upper and the lower mantle but with a steeper shallow segment (model 2 - with lower shortening) (Figure 6). Both experiments share the same mantle flow conditions, only upper plate strength varies. Interestingly, although the slab dip varies (Figure 5D), the deformation rates are constant through time within each one of the experiments (Figure 5B-C). Last, in model 4 (similar background mantle flow conditions, weakest upper plate), both slab geometries are observed on each side of the subducting plate (not imaged on Figure 6 as side pictures are taken only on one side). Despite these differences in slab geometry, the shortening of the upper plate is similar at both plate edges, further suggesting that shortening of the upper plate is primarily controlled by the imposed mantle flow and boundary conditions, rather than by the shape of the slab (Figure 6). Even though we do not discard the idea that flatter slabs favor a stronger coupling between the subducting and overriding plates (e.g., *Molnar and Atwater*, 1978; *Martinod et al.*, 2010, 2020; *Capitanio et al.*, 2011), the slab geometry is found

in our experiments to adjust (in cases variably) to mantle boundary conditions, rather than to be the primarily causal parameter leading to upper plate shortening.

4.2 Comparing our experimental results to a natural case example: the Andean orogeny

The Andes are the most emblematic case of upper plate shortening in a subduction context, and used here as a natural example to further discuss the limitations and strengths of our models. Andean mountain-building is proposed to have been promoted by the westward drift of South America towards the Chile-Peru trench (e.g., *Russo and Silver*, 1994; *Silver et al.*, 1998; *O'Neill et al.*, 2005; *Schellart*, 2008), resulting from the mantle flow associated with the South Atlantic convection cell (e.g., *Husson et al.*, 2012; *Faccenna et al.*, 2013). On the Pacific side, convection mantle models suggest that the Nazca plate is also dragged eastward towards South America (e.g., *Capitanio et al.*, 2011; *Husson*, 2012). Therefore, both the South Atlantic and Pacific convection cells vigorously drag the Nazca and South America plates against each other, together with mantle flow also possibly enhanced by the wide dimensions of the slab or its anchoring into the lower mantle (e.g., *Schellart et al.*, 2007; *Schellart and Moresi*, 2013; *Schellart*, 2017; *Faccenna et al.*, 2017). This results in a positive net trenchward integrated force (e.g., *Husson*, 2012) that possibly led to upper plate shortening and mountain-building along the Andes (e.g., *Capitanio et al.*, 2011; *Schellart*, 2017). Because of experimental limitations, our models cannot precisely reproduce such double mantle convection cells for a proper comparison to the Andes. However, our set-up, where a unidirectional mantle flow drags one plate against the fixed other one, provides an interesting and reasonable alternative to this intrinsic experimental limitation, as the reaction force exerted by the back wall on the fixed plate resists to its mobility and may then be compared to some extent to a force pushing the fixed plate toward the trench (Figure 2). In model 3, mantle flow comes from the upper plate and drives it against the subducting plate. However, in this experiment, shortening is very limited as the trench keeps retreating and the upper plate spreads laterally (Figure 4 and 5). On the contrary, upper plate shortening and thickening are highly favored when the mantle flow drives the oceanic plate against the upper plate, as in models 2, 4 and 5 (Figure 4- 6). In these cases, the trench keeps advancing towards the shortened and thickened upper plate (Figure 6), providing the experimental boundary conditions that best compare here to the Andean context (Figure 8).

Once scaled to natural dimensions, the plate convergence rate is relatively low in our models (~2 cm.yr^{-1} in model 5, Figure 5), when compared to recent Andean conditions (~8 cm.yr^{-1} at ~20°S; *DeMets et al.*, 1994). However, such convergence rates are only obtained experimentally within the boundary conditions favoring upper plate shortening (models 2, 4 and 5) with a fast (10 cm.yr^{-1}) mantle flow. With these experimental conditions, the scaled shortening rate across our modeled upper plate (~0.7 cm.yr^{-1} in model 5) can be compared well to the long-term rate of Andean shortening (~1 cm.yr^{-1} at ~20°S, e.g., *Oncken et al.*, 2006; *Brooks et al.*, 2011). Similarly, the ~33% of upper plate shortening at the end of model 5 (Figure 5 and 7) can be compared well to the total amount of shortening deduced from existing cross-sections across the Andes (>300 km of shortening across the ~650 km wide orogen; Figure 8) (e.g., *Sheffels*, 1990; *Kley and Monaldi*, 1998; *Elger et al.*, 2013; *Barnes and Ehlers*, 2009; *Eichelberger et al.*, 2013). Despite the relatively low convergence rates, our models reproduce shortening rates and amounts that can be compared well to those documented in the Central Andes. This is because upper plate shortening is favored in our models by the weakness of our experimental upper plates, due to their small thickness or to the presence of a weaker silicone as in models 4 and 5. Even though such weak rheologies are not fully realistic, they allow for experimentally producing the conditions that can be compared well, to the first-order, to the deformation observed in nature.

Furthermore, our results suggest that mantle flow dragging the plates against each other has a predominant control on upper plate deformation so that the slab geometry would be an accompanying rather than a causal driving factor for the deformation of the upper plate. In the case of the Andes, the existence of flat slab segments has been invoked to increase the mechanical coupling between the overriding and subducting plates, enhancing the widening of the Andean mountain belt toward the hinterland (e.g., *Ramos et al.*, 2002; *Martinod et al.*, 2010, 2013, 2020; *Horton et al.*, 2022). Slabs would become flatter as a result of their higher positive buoyancy, possibly related to the age of the subducting plate (e.g., *Capitanio et al.*, 2011). Our experiments do not reproduce potential variations in the slab density and cannot be directly compared to these previous works. However, it should be noted that our results indicate that flat slabs are not needed to produce compressive deformation in the upper plate of a subduction zone, even though we cannot discard the possibility that they mechanically favor it. This is in line with recently published detrital data from the Southern Central Andes (~33°S), where propagation of Andean shortening toward the South American hinterland significantly predates that of the flattening of the slab (e.g., *Buelow et al.*, 2018; *Lossada et al.*, 2020), or with the observation that the inboard advance of Andean deformation into the South American continent may also relate to the pre-structuring of the upper plate (e.g., *McQuarrie*, 2002; *Horton et al.*, 2022).

Therefore, even though simple, our experiments

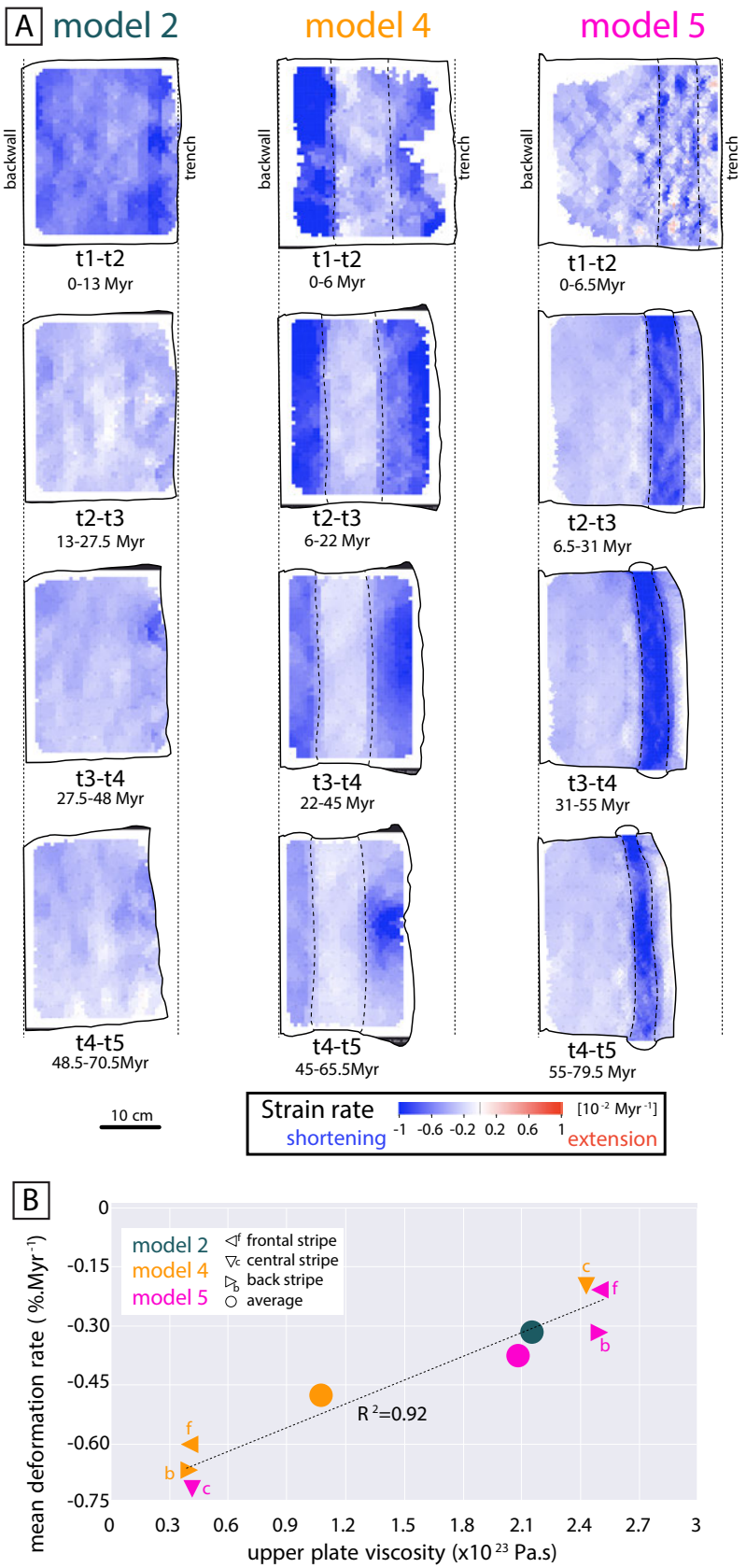

Figure 7 – Deformation recorded for models where the mantle flows toward the upper plate (models 2, 4, and 5). **(A)** Maps showing the strain rate of the short axis of the strain ellipse (in %.Myr^{-1}) for different time intervals, calculated using the SSPX software (e.g., *Cardozo and Allmendinger*, 2009). **(B)** Mean horizontal trench-orthogonal deformation rate as a function of upper plate viscosity. For models 4 and 5, the deformation rate is also calculated for each one of the three silicone stripes (frontal stripe, central stripe, back stripe, as in Figure 6).

satisfactorily reproduce the first-order relative plate boundary conditions and forces that may have led to Andean mountain-building since the Late Cretaceous-Early Cenozoic. Structurally,

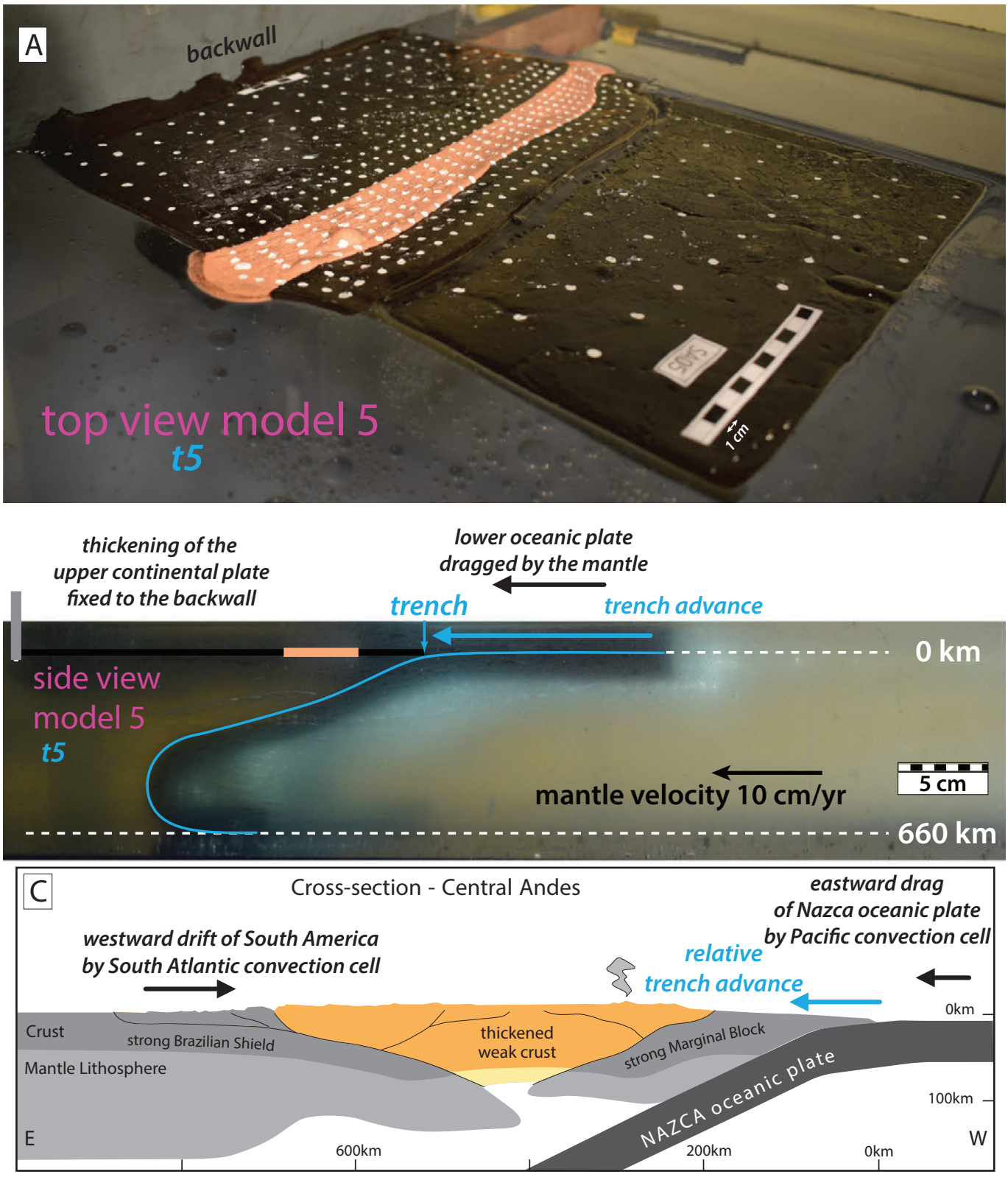

Figure 8 – Comparison between model 5 and the Central Andes. **(A)** Oblique view of the surface of model 5 at t5, showing the oceanic plate on the right and the fixed upper plate on the left. **(B)** Side view of model 5 at t5. **(C)** Schematic cross-section of the Central Andes (modified and adapted from (e.g., *Armijo et al.*, 2015)

the South American subduction margin can be subdivided at ~20–22°S into three main ensembles, from west to east: 1) the Marginal Block, from the subduction trench to the Andean mountain front, including the Coastal Cordillera and the Atacama Bench (after *Armijo et al.*, 2010, 2015); 2) the Andes-Altiplano orogenic system; and 3) the Brazilian Shield (Figure 8C). The Marginal Block and the Brazilian Shield are two relatively rigid ensembles within the upper plate of the subduction margin, barely affected by deformation (e.g., *Wölbern et al.*, 2009; *Lamb*, 2011; *Armijo et al.*, 2015, and

references therein). In contrast, the strong crustal shortening and thickening that lead to the building of the Andes-Altiplano orogenic system localized in between these two relatively rigid features (e.g., *McQuarrie et al.*, 2005; *Oncken et al.*, 2006; *Armijo et al.*, 2015; *Martinod et al.*, 2020). Prior to Andean mountain-building, this particular area of the upper plate endured extension, as recorded by the various Andean Mesozoic Basins (e.g., *Horton*, 2018), leading to its subsequent weakening (e.g., *Armijo et al.*, 2015; *Martinod et al.*, 2020). These initial structural conditions, incorporating a weaker upper plate zone surrounded by two rigid blocks, are best represented by our model 5. In this experiment, we roughly scaled the widths of the three silicone portions to the widths of the three Central Andean blocks. The ~400 km long weaker silicone putty is an analogue of the undeformed initial Andes-Altiplano, surrounded by a narrow (264 km long) stronger continental silicone on the trench side, representing the Marginal Block, and a long (1320 km) stronger silicone block on the continental side, mimicking the Brazilian Shield (Figure 8). Nevertheless, it should be recalled that this analogy only holds to the first order, as silicone behaves as a Newtonian material at low strain rate so that deformation is distributed homogeneously, and cannot localize as in the lithosphere. By using silicones of different viscosities together, with deformation preferentially localized in the weakest part of the continental plate, we highly simplify the nature-like pre-structuring of the Andean continental lithosphere and do not properly mimic the various tectonic ensembles of the Andean orogen in detail (Figure 8). Keeping these simplifications in mind, we nonetheless observe that the weaker silicone simulating the Andes-Altiplano block accommodates more shortening and thickening by a factor 2.3 to 3.6 than the other two blocks. This leads to the building-up of topography within this initially weaker zone of the upper plate of our analogue subduction set-up (Figure 3 and 8).

5 Conclusions

Our experiments show that where plate convergence is not only driven by slab pull but also by a background mantle flow dragging the subducting or overriding plate toward the trench, the continental upper plate deforms. Shortening and thickening are best promoted when the imposed mantle flow is directed toward the overriding plate and when the overriding plate has a no-velocity condition. Indeed, these boundary conditions induce a significant net trench advance, which in turn induces compression in the upper plate. This is a factor required for building an orogenic range in an oceanic subduction context. We also show that the bulk strength of the upper plate is a key factor controlling the amount of shortening in the upper plate. Indeed, the mean deformation rates increase from ~0.3%.Myr^{-1} in model 2 that only includes a stronger lithosphere, to a maximum of ~0.45%.Myr^{-1} in model 4 where the stronger lithosphere only represents one third of the overriding plate. Furthermore, pre-existing structuring of the upper continental plate strongly controls the localization of deformation., as observed deformation rates are around three times larger in the blocks of weaker lithosphere. Our last model (model 5), which includes mantle flow directed toward the fixed upper plate and a weaker block into a stronger lithosphere, is the one that best compares to the Central Andes. In this model, the localization of deformation resembles that of the South American margin, and deformation rates fall in the range of those reconstructed from geological evidences. Taken together, the findings from the experiments presented in this study highlight the importance of mantle drag in building mountains within the upper plates of oceanic subductions.

Acknowledgements

TH benefited from a PhD grant attributed by the French Ministry of Higher Education and Research. This study was supported by grants from the Institut de physique du globe de Paris (IPGP), and partly supported by the IdEx Université de Paris ANR-18-IDEX-0001. We thank Á. Király and an anonymous reviewer for their constructive comments that helped improve this manuscript.

Author contributions

TH, **AR**, **BG**, **MS** and **RL** designed the study and wrote the paper, **JJK** made the experimental setup, **TH**, **AR**, **BG** and **TG** made the experiments in Rennes.

Data availability

A dataset is available and accessible in the open-access repository IPGP Research Collection (https://doi.org/10.18715/IPGP.2023.ldbm60lm). It includes videos depicting the evolution in top and lateral views of the five analogue experiments discussed in this manuscript, as well as five full-resolution pictures at five specific times (t1, t2, t3, t4 and t5) for all these experiments.

Competing interests

No competing interest.

Peer review

This publication was peer-reviewed by Á. Király and an anonymous reviewer. The full peer-review report can be found here: tektonika.online/index.php/home/article/view/25/30

Copyright notice

References

Armijo, R., R. Rauld, R. Thiele, G. Vargas, J. Campos, R. Lacassin, and E. Kausel (2010), The west andean thrust, the san ramon fault, and the seismic hazard for santiago, chile, *Tectonics*, *29*(2), doi: 10.1029/2008tc002427.

Armijo, R., R. Lacassin, A. Coudurier-Curveur, and D. Carrizo (2015), Coupled tectonic evolution of andean orogeny and global climate, *Earth-Science Reviews*, *143*, 1–35, doi: 10.1016/j.earscirev.2015.01.005.

Barnes, J., and T. Ehlers (2009), End member models for andean plateau uplift, *Earth-Science Reviews*, *97*(1-4), 105–132, doi: 10.1016/j.earscirev.2009.08.003.

Brace, W. F., and D. Kohlstedt (1980), Limits on lithospheric stress imposed by laboratory experiments, *Journal of Geophysical Research: Solid Earth*, *85*(B11), 6248–6252, doi: 10.1029/jb085ib11p06248.

Brooks, B. A., M. Bevis, K. Whipple, J. Ramon Arrowsmith, J. Foster, T. Zapata, E. Kendrick, E. Minaya, A. Echalar, M. Blanco, et al. (2011), Orogenic-wedge deformation and potential for great earthquakes in the central andean backarc, *Nature Geoscience*, *4*(6), 380–383, doi: 10.1038/ngeo1143.

Buelow, E., J. Suriano, J. Mahoney, D. Kimbrough, J. F. Mescua, L. B. Giambiagi, and G. D. Hoke (2018), Sedimentologic and stratigraphic evolution of the cacheuta basin: Constraints on the development of the miocene retroarc foreland basin, south-central andes, *Lithosphere*, *10*(3), 366–391, doi: 10.1130/l709.1.

Buffett, B. A. (2006), Plate force due to bending at subduction zones, *Journal of Geophysical Research: Solid Earth*, *111*(B9), doi: 10.1029/2006jb004295.

Capitanio, F., C. Faccenna, S. Zlotnik, and D. Stegman (2011), Subduction dynamics and the origin of andean orogeny and the bolivian orocline, *Nature*, *480*(7375), 83–86, doi: 10.1038/nature10596.

Cardozo, N., and R. W. Allmendinger (2009), Sspx: A program to compute strain from displacement/velocity data, *Computers & Geosciences*, *35*(6), 1343–1357, doi: 10.1016/j.cageo.2008.05.008.

Cerpa, N. G., R. Hassani, M. Gerbault, and J.-H. Prévost (2014), A fictitious domain method for lithosphere-asthenosphere interaction: Application to periodic slab folding in the upper mantle, *Geochemistry, Geophysics, Geosystems*, *15*(5), 1852–1877, doi: 10.1002/2014gc005241.

Cerpa, N. G., B. Guillaume, and J. Martinod (2018), The interplay between overriding plate kinematics, slab dip and tectonics, *Geophysical Journal International*, *215*(3), 1789–1802, doi: 10.1093/gji/ggy365.

Chase, C. G. (1978), Extension behind island arcs and motions relative to hot spots, *Journal of Geophysical Research: Solid Earth*, *83*(B11), 5385–5387, doi: 10.1029/jb083ib11p05385.

Chen, Y.-W., J. Wu, and J. Suppe (2019), Southward propagation of nazca subduction along the andes, *Nature*, *565*, 441–447, doi: 10.1038/s41586-018-0860-1.

Conrad, C. P., and B. H. Hager (1999), Effects of plate bending and fault strength at subduction zones on plate dynamics, *Journal of Geophysical Research: Solid Earth*, *104*(B8), 17,551–17,571, doi: 10.1029/1999JB900149.

Davy, P., and P. Cobbold (1991), Experiments on shortening of a 4-layer model of the continental lithosphere, *Tectonophysics*, *188*(1-2), 1–25, doi: 10.1016/0040-1951(91)90311-f.

DeMets, C., R. G. Gordon, D. F. Argus, and S. Stein (1994), Effect of recent revisions to the geomagnetic reversal time scale on estimates of current plate motions, *Geophysical research letters*, *21*(20), 2191–2194, doi: 10.1029/94gl02118.

Dewey, J. F. (1980), Episodicity, sequence and style at convergent plate boundaries, in *The continental crust and its mineral deposits*, *Geological Association of Canada Special paper*, vol. 20, edited by D. W. Strangway, pp. 553–573.

Duarte, J. C., W. P. Schellart, and A. R. Cruden (2014), Rheology of petrolatum–paraffin oil mixtures: applications to analogue modelling of geological processes, *Journal of Structural Geology*, *63*, 1–11, doi: 10.1016/j.jsg.2014.02.004.

Duarte, J. C., W. P. Schellart, and A. R. Cruden (2015), How weak is the subduction zone interface?, *Geophysical Research Letters*, *42*(8), 2664–2673, doi: 10.1002/2014gl062876.

Dvorkin, J., A. Nur, G. Mavko, and Z. Ben-Avraham (1993), Narrow subducting slabs and the origin of backarc basins, *Tectonophysics*, *227*(1-4), 63–79, doi: 10.1016/0040-1951(93)90087-Z.

Eichelberger, N., N. McQuarrie, T. A. Ehlers, E. Enkelmann, J. B. Barnes, and R. O. Lease (2013), New constraints on the chronology, magnitude, and distribution of deformation within the central andean orocline, *Tectonics*, *32*(5), 1432–1453, doi: 10.1002/tect.20073.

Elger, K., O. Oncken, and J. Glodny (2013), Plateau-style accumulation of deformation: Southern altiplano, *Tectonics*, *24*(4), TC4020, doi: 10.1029/2004TC001675.

England, P., and D. McKenzie (1982), A thin viscous sheet model for continental deformation, *Geophysical Journal International*, *70*(2), 295–321, doi: 10.1111/j.1365-246x.1982.tb04969.x.

Faccenna, C., T. W. Becker, C. P. Conrad, and L. Husson (2013), Mountain building and mantle dynamics, *Tectonics*, *32*(1), 80–93, doi: 10.1029/2012TC003176.

Faccenna, C., O. Oncken, A. F. Holt, and T. W. Becker (2017), Initiation of the andean orogeny by lower mantle subduction, *Earth and Planetary Science Letters*, *463*, 189–201, doi: 10.1016/j.epsl.2017.01.041.

Funiciello, F., C. Faccenna, D. Giardini, and K. Regenauer-Lieb (2003), Dynamics of retreating slabs: 2. insights from three-dimensional laboratory experiments, *Journal of Geophysical Research: Solid Earth*, *108*(B4), doi: 10.1029/2001JB000896.

Funiciello, F., C. Faccenna, and D. Giardini (2004), Role of lateral mantle flow in the evolution of subduction systems: insights from laboratory experiments, *Geophysical Journal International*, *157*(3), 1393–1406, doi: 10.1111/j.1365-246X.2004.02313.x.

Garfunkel, Z., C. Anderson, and G. Schubert (1986), Mantle circulation and the lateral migration of subducted slabs, *Journal of Geophysical Research: Solid Earth*, *91*(B7), 7205–7223, doi: 10.1029/JB091iB07p07205.

Gibert, G., M. Gerbault, R. Hassani, and E. Tric (2012), Dependency of slab geometry on absolute velocities and conditions for cyclicity: insights from numerical modelling, *Geophysical Journal International*, *189*(2), 747–760, doi: 10.1111/j.1365-246x.2012.05426.x.

Guillaume, B., J. Martinod, and N. Espurt (2009), Variations of slab dip and overriding plate tectonics during subduction: Insights from analogue modelling, *Tectonophysics*, *463*(1-4), 167–174, doi: 10.1016/j.tecto.2008.09.043.

Guillaume, B., S. Hertgen, J. Martinod, and N. G. Cerpa (2018), Slab dip, surface tectonics: How and when do they change following an acceleration/slow down of the overriding plate?, *Tectonophysics*, *726*, 110–120, doi: 10.1016/j.tecto.2018.01.030.

Guillaume, B., F. Funiciello, and C. Faccenna (2021), Interplays between mantle flow and slab pull at subduction zones in 3d, *Journal of Geophysical Research: Solid Earth*, *126*(5), e2020JB021,574, doi: 10.1029/2020jb021574.

Habel, T. (2022), Contribution of the west andean flank in northern chile to early stages of the andean orogeny: Insights from structural geology, thermochronology and analog modeling, Ph.D. thesis.

Hayes, G. P., G. L. Moore, D. E. Portner, M. Hearne, H. Flamme, M. Furtney, and G. M. Smoczyk (2018), Slab2, a comprehensive subduction zone geometry model, *Science*, *362*(6410), 58–61, doi: 10.1126/science.aat4723.

Heuret, A., and S. Lallemand (2005), Plate motions, slab dynamics and back-arc deformation, *Physics of the Earth and Planetary Interiors*, *149*(1-2), 31–51, doi: 10.1016/j.pepi.2004.08.022.

Holt, A. F., T. Becker, and B. Buffett (2015), Trench migration and overriding plate stress in dynamic subduction models, *Geophysical Journal International*, *201*(1), 172–192, doi: 10.1093/gji/ggv011.

Horton, B. K. (2018), Tectonic regimes of the central and southern andes: Responses to variations in plate coupling during subduction, *Tectonics*, *37*(2), 402–429, doi: 10.1002/2017tc004624.

Horton, B. K., T. N. Capaldi, and N. D. Perez (2022), The role of flat slab subduction, ridge subduction, and tectonic inheritance in andean deformation, *Geology*, *50*(9), 1007–1012, doi: 10.1130/G50094.1.

Husson, L. (2012), The dynamics of plate boundaries over a convecting mantle, *Physics of the Earth and Planetary Interiors*, *212*, 32–43, doi: 10.1016/j.pepi.2012.09.006.

Husson, L., C. P. Conrad, and C. Faccenna (2012), Plate motions, andean orogeny, and volcanism above the south atlantic convection cell, *Earth and Planetary Science Letters*, *317*, 126–135, doi: 10.1016/j.epsl.2011.11.040.

Jaillard, E., G. Hérail, T. Monfret, E. Díaz-Martínez, P. Baby, A. Lavenu, J.-F. Dumont, U. Cordani, E. Milani, D. Campos, et al. (2000), Tectonic evolution of the andes of ecuador, peru, bolivia and northern chile, in *Tectonic evolution of South America*, edited by U. G. Cordani, E. J. Milani, A. Thomaz Filho, and D. A. Campos, 31st International Geological Congress, pp. 481–559, Rio de Janeiro, Brazil.

Király, Á., F. A. Capitanio, F. Funiciello, and C. Faccenna (2017), Subduction induced mantle flow: Length-scales and orientation of the toroidal cell, *Earth and Planetary Science Letters*, *479*, 284–297, doi: 10.1016/j.epsl.2017.09.017.

Kley, J., and C. R. Monaldi (1998), Tectonic shortening and crustal thickness in the central andes: How good is the correlation?, *Geology*, *26*(8), 723–726, doi: 10.1130/0091-7613(1998)026<0723:tsacti>2.3.co;2.

Lallemand, S., A. Heuret, and D. Boutelier (2005), On the relationships between slab dip, back-arc stress, upper plate absolute motion, and crustal nature in subduction zones, *Geochemistry, Geophysics, Geosystems*, *6*(9), doi: 10.1029/2005gc000917.

Lamb, S. (2011), Did shortening in thick crust cause rapid late cenozoic uplift in the northern bolivian andes?, *Journal of the Geological Society*, *168*(5), 1079–1092, doi: 10.1144/0016-76492011-008.

Lossada, A. C., G. D. Hoke, L. B. Giambiagi, P. Fitzgerald, J. F. Mescua, J. Suriano, and A. Aguilar (2020), Detrital thermochronology reveals major middle miocene exhumation of the eastern flank ofthe andes that predates the pampeanflat slab (33–33.5 s), *Tectonics*, *39*(4), e2019TC005,764, doi: 10.1029/2019tc005764.

Martinod, J., F. Funiciello, C. Faccenna, S. Labanieh, and V. Regard (2005), Dynamical effects of subducting ridges: insights from 3-d laboratory models, *Geophysical Journal International*, *163*(3), 1137–1150, doi: 10.1111/j.1365-246x.2005.02797.x.

Martinod, J., L. Husson, P. Roperch, B. Guillaume, and N. Espurt (2010), Horizontal subduction zones, convergence velocity and the building of the andes, *Earth and Planetary Science Letters*, *299*(3-4), 299–309, doi: 10.1016/j.epsl.2010.09.010.

Martinod, J., B. Guillaume, N. Espurt, C. Faccenna, F. Funiciello, and V. Regard (2013), Effect of aseismic ridge subduction on slab geometry and overriding plate deformation: Insights from analogue modeling, *Tectonophysics*, *588*, 39–55, doi: 10.1016/j.tecto.2012.12.010.

Martinod, J., M. Gérault, L. Husson, and V. Regard (2020), Widening of the andes: An interplay between subduction dynamics and crustal wedge tectonics, *Earth-Science Reviews*, *204*, 103,170, doi: 10.1016/j.earscirev.2020.103170.

McQuarrie, N. (2002), The kinematic history of the central andean fold-thrust belt, bolivia: Implications for building a high plateau, *Geological Society of America Bulletin*, *114*(8), 950–963, doi: 10.1130/0016-7606(2002)114<0950:tkhotc>2.0.co;2.

McQuarrie, N., B. K. Horton, G. Zandt, S. Beck, and P. G. DeCelles (2005), Lithospheric evolution of the andean fold–thrust belt, bolivia, and the origin of the central andean plateau, *Tectonophysics*, *399*(1-4), 15–37, doi: 10.1016/j.tecto.2004.12.013.

Meyer, C., and W. P. Schellart (2013), Three-dimensional dynamic models of subducting plate-overriding plate-upper mantle interaction, *Journal of Geophysical Research: Solid Earth*, *118*(2), 775–790, doi: 10.1002/jgrb.50078.

Mitrovica, J., and A. Forte (2004), A new inference of mantle viscosity based upon joint inversion of convection and glacial isostatic adjustment data, *Earth and Planetary Science Letters*, *225*(1-2), 177–189, doi: 10.1016/j.epsl.2004.06.005.

Molnar, P., and T. Atwater (1978), Interarc spreading and cordilleran tectonics as alternates related to the age of subducted oceanic lithosphere, *Earth and Planetary Science Letters*, *41*(3), 330–340, doi: 10.1016/0012-821x(78)90187-5.

Mpodozis, C., and V. Ramos (1990), The andes of chile and argentina, in *Geology of the Andes and its Relation to Hydrocarbon and Mineral Resources*, edited by G. E. Ericksen, M. T. Cañas Pinochet, and J. A. Reinemund, Circum-Pacific Council for Energy and Mineral Resources Earth Sciences Series, pp. 59–90, Circum Pacific Council Publications, Houston, Texas.

Müller, R. D., M. Seton, S. Zahirovic, S. E. Williams, K. J. Matthews, N. M. Wright, G. E. Shephard, K. T. Maloney, N. Barnett-Moore, M. Hosseinpour, et al. (2016), Ocean basin evolution and global-scale plate reorganization events since pangea breakup, *Annual Review of Earth and Planetary Sciences*, *44*, 107–138, doi: 10.1146/annurev-earth-060115-012211.

Oncken, O., D. Hindle, J. Kley, K. Elger, P. Victor, and K. Schemmann (2006), Deformation of the central andean upper plate system — facts, fiction, and constraints for plateau models, in *The Andes: Active Subduction Orogeny*, edited by O. Oncken, G. Chong, G. Franz, P. Giese, H.-J. Götze, V. A. Ramos, M. R. Strecker, and P. Wigger, pp. 3–27, Springer, Berlin, Germany, doi: 10.1007/978-3-540-48684-8_1.

O'Neill, C., D. Müller, and B. Steinberger (2005), On the uncertainties in hot spot reconstructions and the significance of moving hot spot reference frames, *Geochemistry, Geophysics, Geosystems*, *6*(4), Q04,003, doi: 10.1029/2004GC000784.

Quinteros, J., and S. V. Sobolev (2013), Why has the nazca plate slowed since the neogene?, *Geology*, *41*(1), 31–34, doi: 10.1130/g33497.1.

Ramos, V. A., E. O. Cristallini, and D. J. Pérez (2002), The pampean flat-slab of the central andes, *Journal of South American earth sciences*, *15*(1), 59–78, doi: 10.1016/S0895-9811(02)00006-8.

Ranalli, G. (1995), *Rheology of the Earth*, Springer Science & Business Media.

Replumaz, A., F. Funiciello, R. Reitano, C. Faccenna, and M. Balon (2016), Asian collisional subduction: A key process driving formation of the tibetan plateau, *Geology*, *44*(11), 943–946, doi: 10.1130/G38276.1.

Richards, M. A., and D. C. Engebretson (1992), Large-scale mantle convection and the history of subduction, *Nature*, *355*(6359), 437–440, doi: 10.1038/355437a0.

Rudolf, M., D. Boutelier, M. Rosenau, G. Schreurs, and O. Oncken (2016), Rheological benchmark of silicone oils used for analog modeling of short-and long-term lithospheric deformation, *Tectonophysics*, *684*, 12–22, doi: 10.1016/j.tecto.2015.11.028.

Russo, R., and P. Silver (1994), Trench-parallel flow beneath the nazca plate from seismic anisotropy, *Science*, *263*(5150), 1105–1111, doi: 10.1126/science.263.5150.1105.

Schellart, W. P. (2008), Overriding plate shortening and extension above subduction zones: A parametric study to explain formation of the andes mountains, *Geological Society of America Bulletin*, *120*(11-12), 1441–1454, doi: 10.1130/B26360.1.

Schellart, W. P. (2011), Rheology and density of glucose syrup and honey: Determining their suitability for usage in analogue and fluid dynamic models of geological processes, *Journal of Structural Geology*, *33*(6), 1079–1088, doi: 10.1016/j.jsg.2011.03.013.

Schellart, W. P. (2017), Andean mountain building and magmatic arc migration driven by subduction-induced whole mantle flow, *Nature communications*, *8*(1), 2010, doi: 10.1038/s41467-017-01847-z.

Schellart, W. P., and L. Moresi (2013), A new driving mechanism for backarc extension and backarc shortening through slab sinking induced toroidal and poloidal mantle flow: Results from dynamic subduction models with an overriding plate, *Journal of Geophysical Research: Solid Earth*, *118*(6), 3221–3248, doi: 10.1002/jgrb.50173.

Schellart, W. P., J. Freeman, D. R. Stegman, L. Moresi, and D. May (2007), Evolution and diversity of subduction zones controlled by slab width, *Nature*, *446*(7133), 308–311, doi: 10.1038/nature05615.

Sheffels, B. M. (1990), Lower bound on the amount of crustal shortening, in the central bolivian andes, *Geology*, *18*(9), 812–815, doi: 10.1130/0091-7613(1990)018<0812:lbotao>2.3.co;2.

Silver, P. G., R. M. Russo, and C. Lithgow-Bertelloni (1998), Coupling of south american and african plate motion and plate deformation, *Science*, *279*(5347), 60–63, doi: 10.1126/science.279.5347.60.

Sobolev, S. V., and A. Y. Babeyko (2005), What drives orogeny in the andes?, *Geology*, *33*(8), 617–620, doi: 10.1130/g21557ar.1.

Strak, V., and W. P. Schellart (2016), Control of slab width on subduction-induced upper mantle flow and associated upwellings: Insights from analog models, *Journal of Geophysical Research: Solid Earth*, *121*(6), 4641–4654, doi: 10.1002/2015jb012545.

Turcotte, D. L., and G. Schubert (2002), *Geodynamics*, Cambridge university press.

Uyeda, S., and H. Kanamori (1979), Back-arc opening and the mode of subduction, *Journal of Geophysical Research: Solid Earth*, *84*(B3), 1049–1061, doi: 10.1029/jb084ib03p01049.

Wölbern, I., B. Heit, X. Yuan, G. Asch, R. Kind, J. Viramonte, S. Tawackoli, and H. Wilke (2009), Receiver function images from the moho and the slab beneath the altiplano and puna plateaus in the central andes, *Geophysical Journal International*, *177*(1), 296–308, doi: 10.1111/j.1365-246x.2008.04075.x.

Wolf, S. G., and R. S. Huismans (2019), Mountain building or backarc extension in ocean-continent subduction systems: A function of backarc lithospheric strength and absolute plate velocities, *Journal of Geophysical Research: Solid Earth*, *124*(7), 7461–7482, doi: 10.1029/2018jb017171.

Zhong, S., and M. Gurnis (1994), Controls on trench topography from dynamic models of subducted slabs, *Journal of Geophysical Research: Solid Earth*, *99*(B8), 15,683–15,695, doi: 10.1029/94JB00809.